AAS 25-186

THE ROLE OF AUTONOMY IN CLOSE PROXIMITY OPERATIONS AROUND ASTEROID (99942) APOPHIS

Carmine Buonagura[*], Saptarshi Bandyopadhyay[†], Bonan Zhou[‡], Benjamin J. Hockman[§], Jacopo Villa[¶], Issa Nesnas[‖], Francesco Topputo[**], Steven Ardito[††]

Asteroid exploration is rapidly advancing, but challenges such as environmental uncertainties, communication delays, and high costs complicate missions in close proximity to these bodies. Autonomy offers robust solutions for real-time decision-making and is increasingly being implemented on platforms with limited capabilities, such as CubeSats, which allow for riskier operations due to their low costs. This study uses the Multi-Spacecraft Concept and Autonomy Tool (MuSCAT) simulator to model the 6U Distributed Radar Observations of Interior Distributions (DROID) spacecraft mission near asteroid (99942) Apophis, focusing on attitude and orbital estimation and control, while considering different orbital distances and thrusting errors. The work identifies a one-day interval between trajectory correction maneuvers as a practical limit to avoid the need for autonomy and aims to determine when autonomy becomes necessary for efficient asteroid missions.

INTRODUCTION

Asteroid exploration is experiencing rapid growth due to various motivations, including scientific research, planetary defense, and resource exploitation.[1–3] However, operating in the vicinity of these small bodies presents numerous challenges. Key difficulties include environmental uncertainties, communication delays, and high costs associated with ground-in-the-loop operations. Uncertainties near asteroids are particularly diverse. Firstly, these bodies are not well characterized from ground-based observations,[4] indeed their shape and morphology are often poorly known, as

[*]Research Intern, Jet Propulsion Laboratory, California Institute of Technology, 4800 Oak Grove Dr, Pasadena, CA 91109 USA.
PhD Student, Department of Aerospace Science and Technology, Politecnico di Milano, Via La Masa 34, 20156, Milan, Italy.
[†]Robotics Technologist, Jet Propulsion Laboratory, California Institute of Technology, 4800 Oak Grove Dr, Pasadena, CA 91109 USA.
[‡]Guidance and Control Engineer, Jet Propulsion Laboratory, California Institute of Technology, 4800 Oak Grove Dr, Pasadena, CA 91109 USA.
[§]Robotics Technologist, Jet Propulsion Laboratory, California Institute of Technology, 4800 Oak Grove Dr, Pasadena, CA 91109 USA.
[¶]Research Assistant, Aerospace Engineering Sciences, University of Colorado Boulder, 3775 Discovery Drive, Boulder, CO 80303 USA.
[‖]Robotics Technologist, Jet Propulsion Laboratory, California Institute of Technology, 4800 Oak Grove Dr, Pasadena, CA 91109 USA.
[**]Full Professor, Department of Aerospace Science and Technology, Politecnico di Milano, Via La Masa 34, 20156, Milan, Italy.
[††]Chief Engineer, Engineering Development Office, Jet Propulsion Laboratory, California Institute of Technology, 4800 Oak Grove Dr, Pasadena, CA 91109 USA.

demonstrated by missions like Double Asteroid Redirection Test (DART),[5,6] Rosetta,[7] and Origins, Spectral Interpretation, Resource Identification, and Security – Regolith Explorer (OSIRIS-REx).[8] Additionally, the dynamics in the proximity of minor bodies is highly nonlinear due to their irregular shapes, the non-uniform mass distribution throughout the asteroid volume, and the presence of unpredictable perturbations such as the Solar Radiation Pressure (SRP). These uncertainties impact the entire Guidance, Navigation, and Control (GNC) subsystem, requiring its design to be robust against the aforementioned challenges.

Communication delays can range from a few seconds to several minutes,[9] depending on the small body considered. These delays pose significant challenges, particularly in situations where real-time decision-making and control are required. The further the spacecraft is from Earth, the longer the communication delay, making it crucial for onboard systems to handle GNC independently during critical operations near asteroids.

Additionally, high costs are related to maintaining an on-ground operations team that is always available to process incoming data. This team must monitor the spacecraft status, analyze data, and make critical adjustments in response to evolving mission conditions. The need for continuous human oversight is extremely time-consuming, especially during complex operations near asteroids, where readiness for any unexpected events must be ensured.

Even though previous asteroid missions have relied on regular communications between the spacecraft and the ground operations team,[10–13] autonomy has become a significant focus in addressing these challenges, offering advantages such as adaptability and real-time decision-making, which increase mission efficiency without waiting for instructions from Earth. These capabilities are especially valuable in the nonlinear and highly uncertain environment near asteroids. Autonomous systems can promptly react to unexpected events and make decisions that would be impractical to handle from a ground station, thereby increasing the likelihood of mission success. Nonetheless, it is essential to recognize that autonomy is not always the optimal solution. Developing and testing these autonomous systems is complex and expensive, requiring significant time and resources to ensure robustness across various scenarios and unexpected situations. The integration of autonomous algorithms also carries risks, such as the possibility of making suboptimal decisions without human oversight. Therefore, a careful analysis of the potential benefits versus the risks and costs of implementing autonomy is necessary. Additionally, autonomous algorithms are not implemented on medium and large spacecraft due to a lack of trust in these methods and the high manufacturing and launch costs for such satellites, which cannot perform risky operations that could jeopardize the mission. For this reason, there is an increasing use of cost-effective platforms like CubeSats for minor body close-proximity operations. These platforms operate with limited onboard resources and maneuvering capabilities, yet they are favored due to their reduced manufacturing costs and ease of launch, which allow for riskier missions. An example is the Hera mission,[14] which includes CubeSats like Milani[15] and Juventas,[16] set to approach the binary asteroid (65803) Didymos in 2027. While these platforms effectively reduce mission costs, they significantly complicate the onboard implementation of autonomous algorithms due to their constrained resources. Therefore, identifying the specific conditions under which autonomy is necessary for CubeSats in close-proximity operations is crucial.[17]

This study utilizes the Multi-Spacecraft Concept and Autonomy Tool, a mission-level multi-subsystem simulator, to model spacecraft orbiting different trajectories around a variety of asteroids differing in size, density, and shape. The tool enables the simulation of trajectory evolution coupled with attitude modeling. Consequently, the choice of spacecraft and the selection of the nominal

trajectory significantly affects the simulation results. For this study, the focus is on the 6U CubeSat designed for the DROID mission,[18,19] which will operate in close proximity to asteroid (99942) Apophis alongside a twin spacecraft to observe tidal deformations of the asteroid during its 2029 close encounter with Earth. The mission objective is to characterize (99942) Apophis internal structure through monostatic and bistatic radar measurements. In this work, the CubeSat is assumed to follow a quasi-terminator polar orbit as its nominal trajectory. To thoroughly assess how well the spacecraft can maintain its trajectory and attitude in the complex environment near the asteroid, various factors are considered, including different orbital distances from the asteroid, variations in thrusting errors, and diverse orbital control strategies.
State-of-the-art methods for attitude and orbital estimation and control are employed. Specifically, attitude estimation is performed employing an Extended Kalman Filter (EKF) using Inertial Measurement Unit (IMU), star tracker and sun sensor measurements. Attitude control is based on a non-linear tracking control strategy and uses micro-thrusters and reaction wheels. Orbital estimation is achieved using an EKF with simulated optical measurements and knowledge of landmarks on the asteroid's surface, while orbital control is executed through a Lambert maneuver, involving two consecutive burns with a chemical thruster: a position and velocity phasing burn.

Most NASA missions maintain a daily cadence of ground operations, which refers to the time interval between data downlink (from spacecraft to ground station) and command uplink (from ground station to spacecraft). Consequently, this one-day interval has been considered the minimum time between TCMs to avoid the need for onboard spacecraft autonomy. In this work, this one-day time interval will be referred to as the cadence of ground operations.

This paper lays the groundwork for establishing the foundational understanding required to determine the conditions under which spacecraft autonomy becomes essential. By exploring these parameters, we aim to enhance the efficiency and success of future close-proximity asteroid missions.

Literature Survey

Autonomous GNC algorithms have been extensively studied in the literature, particularly for challenging and uncertain environments near minor bodies. However, previous studies have often employed a point mass model for the spacecraft, overlooking the significant influence of attitude perturbations and control actions on its orbital dynamics. They have also not accounted for the actual sensors and actuators present on the spacecraft, nor considered relevant disturbances on spacecraft attitude, such as reaction wheels desaturation.

Negri[9] implements robust guidance and control algorithms that directly handle uncertainties during the approach and hovering phases of asteroids (101955) Bennu and (433), avoiding the need for extensive navigation campaigns. This work also employs the cannonball model to account for the SRP.

In contrast, Takahashi[20] simulates the approach and hovering of (101955) Bennu using autonomous navigation and orbit control. In this study, the true SRP is simulated with a hypothetical spacecraft, assuming that the solar panels can always face the sun. Other works, from Furfaro,[21,22] have implemented nonlinear landing and hovering schemes for real-time onboard use, treating the spacecraft as a point mass.

Various studies have also been conducted on autonomous navigation for asteroids,[23–25] covering different mission phases, from approach to landing.

All the aforementioned works propose guidance, navigation, and control laws that can support autonomous operations. However, they use simplified attitude models, do not model sensors and actuators, and do not critically assess the actual need for autonomy.

French[26] addresses the need for autonomy in performing bistatic radar measurements of (99942) Apophis. The orbital control strategy in this case involves maintaining the angle between the two spacecraft position vectors, relative to the asteroid center of mass, below 7.5 deg. This work uses the high-fidelity simulator Mission Analysis, Operations, and Navigation Toolkit Environment (MONTE) for spacecraft orbit determination with realistic flight-like data cut-off, representing the time interval between data downlink and the processing of that data by the ground operations center. However, spacecraft attitude is not modeled, and the cannonball model is used to calculate the SRP.

In this work, we aim to simulate all the spacecraft subsystems by coupling trajectory modeling with attitude effects to assess the conditions under which autonomy becomes necessary.

Main Contributions

The primary focus of this work is the enhancement of two critical spacecraft subsystems within MuSCAT: the navigation subsystem and the attitude determination and control subsystem. Four state-of-the-art algorithms were implemented and integrated within the tool: attitude estimation, attitude control, orbit determination, and orbit control. These algorithms are used to simulate the orbital and attitude dynamics of a CubeSat around asteroid (99942) Apophis. In this work, the spacecraft is not considered as a point mass, but its attitude dynamics is also considered, playing an important role on trajectory modeling.

The secondary focus is spacecraft autonomy, which is the key aspect of this work. This study will assess different spacecraft orbital distances from the asteroid, along with varying thrusting errors, to evaluate the frequency of Trajectory Correction Maneuvers (TCM) and assess the extent to which autonomy is needed for proximity operations around asteroids. It can be concluded that the implementation of autonomous algorithms requires extensive validation and testing. Therefore, when not essential, spacecraft operations could be simplified by utilizing ground-based orbital control.

The main outcome of this work is the assessment of the orbital distances at which spacecraft autonomy is not needed for asteroid (99942) Apophis, depending on the propulsion system thrusting error and the control strategy employed to keep the spacecraft aligned with the nominal trajectory.

Paper Organization

The paper is organized as follows. In the initial part of the study, a detailed description of the problem statement is presented. Following this, the algorithms implemented in MuSCAT are thoroughly described and the simulation setup and study results for asteroid (99942) Apophis are presented. Finally, the study concludes with a discussion of some final considerations and future work.

PROBLEM STATEMENT

The term autonomy, according to the Jet Propulsion Laboratory (JPL) autonomy strategic plan, is defined as:

> *"Making decisions and taking actions, in the presence of uncertainty, to execute the mission and respond to internal and external changes without human intervention"*

Close proximity operations near asteroids require rapid responses due to the uncertainties and non-linearities inherently present in these challenging environments. Therefore, it is essential to determine the extent to which a spacecraft can rely on ground-based commands and when autonomy becomes necessary, as human intervention may take too long and be incompatible with the fast evolving dynamics.
The problem to be addressed is to determine the range of distances at which spacecraft autonomy becomes necessary during asteroids close proximity operations in the presence of thrust errors. Autonomy is considered essential when the frequency of TCMs falls below 1 per day, which is the minimum cadence of ground operations for most NASA missions.
The following paragraphs will provide an in-depth discussion of the asteroid, spacecraft, and orbit characteristics considered in this paper.

Asteroid Asteroid (99942) Apophis is an elongated and irregular shaped near-Earth asteroid that will pass close to Earth on April 13, 2029.[27] This asteroid has garnered significant attention because its close approach presents a unique opportunity for scientists to study its properties, orbit, and potential risks for future encounters. In this work, the radar shape model of (99942) Apophis is used for simulations.[28,29] The spherical harmonics gravity model used in this work is based on the actual model computed from Brozovic,[28] which considers an equivalent radius of $221.6\ \mathrm{m}$ and a gravitational constant of $3 \times 10^{-9}\ \mathrm{km}^3/\mathrm{s}^2$ assuming a constant density across its volume. Its spin axis orientation is assumed to have a right ascension and declination of $250\ \mathrm{deg}$ and $-75\ \mathrm{deg}$, respectively, with a rotation period of $27.38\ \mathrm{h}$. Throughout the simulations, (99942) Apophis gravity field will be modeled using spherical harmonics expansions up to the 8^{th} order. All the relevant asteroid properties are shown in Table 1.

Table 1: Relevant (99942) Apophis properties.

R_{eq} [m]	μ [$\mathrm{km}^3/\mathrm{s}^2$]	Pole RA [deg]	Pole Dec [deg]	Pole Period [h]
221.6	3×10^{-9}	250	-75	27.38

Spacecraft The spacecraft considered in this paper is the 6U CubeSat designed for the DROID mission. The DROID CubeSat, shown in Figure 1, is $0.3\,\mathrm{m} \times 0.2\,\mathrm{m} \times 0.1\,\mathrm{m}$ in volume, with a total dry mass of $14\,\mathrm{kg}$ and total propellant mass of $1\,\mathrm{kg}$. It is equipped with 2 passive deployed solar panels, with a total area of $0.24\ \mathrm{m}^2$ and a reflectivity coefficient α equal to 0.6. The absence of solar panels gimbals means that attitude control is required to orient the solar panels to face the Sun whenever power is needed for its subsystems. The spacecraft and solar panel properties are reported in Table 2.

Table 2: Relevant DROID 6U CubeSat properties.

m_{SC} [kg]	$A_{\text{SC}_{\text{max}}}$ [m^2]	$A_{\text{SP}_{\text{max}}}$ [m^2]	α [$-$]
15	0.03	0.24	0.6

The CubeSat is equipped with a set of sensors and actuators: specifically, one star tracker, one sun sensor, and one IMU are used for attitude estimation; 12 micro-thrusters and 3 reaction wheels are employed for attitude control; and a chemical thruster is used for orbital control. Finally, a

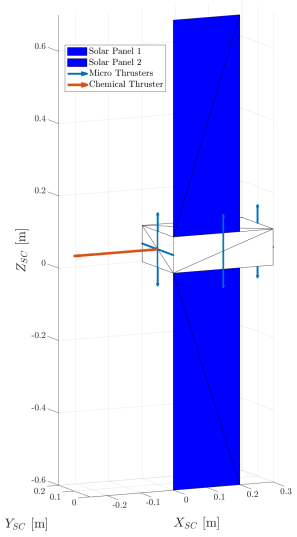

Figure 1: DROID 6U CubeSat

navigation camera is used for scientific observations and orbit determination. Table 3 shows all the usefull properties of sensors, actuators, and instruments onboard the spacecraft.

Table 3: Sensors, actuators, and instruments used onboard the DROID CubeSat.

Sensors		**Actuators**		**Instruments**	
Star tracker		**Micro-thruster**		**Camera**	
Number	1	Number	12	Number	1
Orientation	[1, 0, 0]	Thrust	0.01 N	Orientation	[1, 0, 0]
Frequency	10 Hz	Noise	10^{-4} N	Frequency	20 Hz
Noise	0.012 deg	Specific Impulse	50 s	Field of View	50 deg
				Resolution	[1024 1024] pxl
Sun sensor		**Reaction wheel**			
Number	1	Number	3		
Orientation	[1, 0, 0]	Radius	0.0215 m		
Frequency	1 Hz	Mass	0.137 kg		
Noise	0.5 deg	Angular velocity	6500 RPM		
IMU		**Chemical thruster**			
Number	1	Number	1		
Noise	5.6×10^{-3} deg/s	Orientation	[1, 0, 0]		
Frequency	10 Hz	Max thrust	1 N		
Biases	[0.05 0.06 0.07] deg/s	Specific Impulse	200 s		

Trajectory Minor body close-proximity operations involve different types of orbits, such as Sun-stabilized terminator orbits (SSTO), hyperbolic trajectories, periodic orbits, retrograde equatorial orbits, and others. The choice of the most favorable nominal trajectory depends strongly on the characteristics of the asteroid and the operational distance of the spacecraft. To perform a broadly

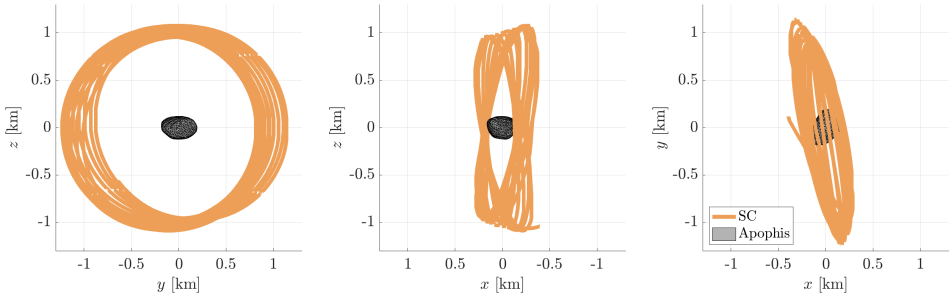

Figure 2: Nominal trajectory of DROID over 20 days of simulation.

applicable analysis, a quasi-polar terminator orbit has been assumed. This orbit has been generated considering a central gravity field and a constant equivalent SRP acting on the spacecraft. Specifically, it is assumed that the maximum area of the spacecraft, including both solar panels and the maximum CubeSat face, is exposed to a constant Sun incidence angle of 45 deg.

$$A_{\text{eq}} = \frac{A_{\text{SC}_{\text{max}}} + A_{\text{SP}_{\text{max}}}}{\sqrt{2}} \tag{1}$$

The reflectivity coefficient α has been set equal to that of the solar panels, with a value of 0.6. The nominal trajectory has been generated considering an initial position on a plane perpendicular to the Sun-asteroid vector and passing through the asteroid center of mass. Note that this orbit differs from common SSTOs, which were not considered due to their lack of flexibility, as they can only be generated under limited conditions and depend on the specific spacecraft properties. The distance from the asteroid is varied, while the velocity at the starting point is assumed to be equal to the Keplerian circular velocity at the given distance. Along this trajectory, the scientific goal of the spacecraft is to capture images of the asteroid for both scientific and navigation purposes. Consequently, the spacecraft has to point its navigation camera toward the asteroid as much as possible.

IMPLEMENTATION IN MUSCAT

All the results presented in this paper are generated using MuSCAT.[30,31] MuSCAT is a Matlab-based integrated platform designed for low-fidelity simulations of single or multiple spacecraft in cruise or orbit. It simulates interactions among spacecraft subsystems with first-order accuracy. The subsystems modeled by MuSCAT include navigation, attitude determination and control, power management, communications, data handling, and science instruments. MuSCAT facilitates spacecraft architecture evaluation, autonomy trade studies, and end-to-end simulations of minor body missions. Figure 3 illustrates the tool's data flow, which is organized into two primary layers: the Autonomous Flight Software and the Physics-based Simulation.

Autonomous Flight Software The Autonomous Flight Software layer is further divided into two sublayers. The System-level Onboard Autonomy layer is responsible for scheduling and executing tasks, such as orbital control, power managements, and reaction wheels desaturation. The Functional-level Onboard Autonomy layer manages all spacecraft subsystems. The functional layer

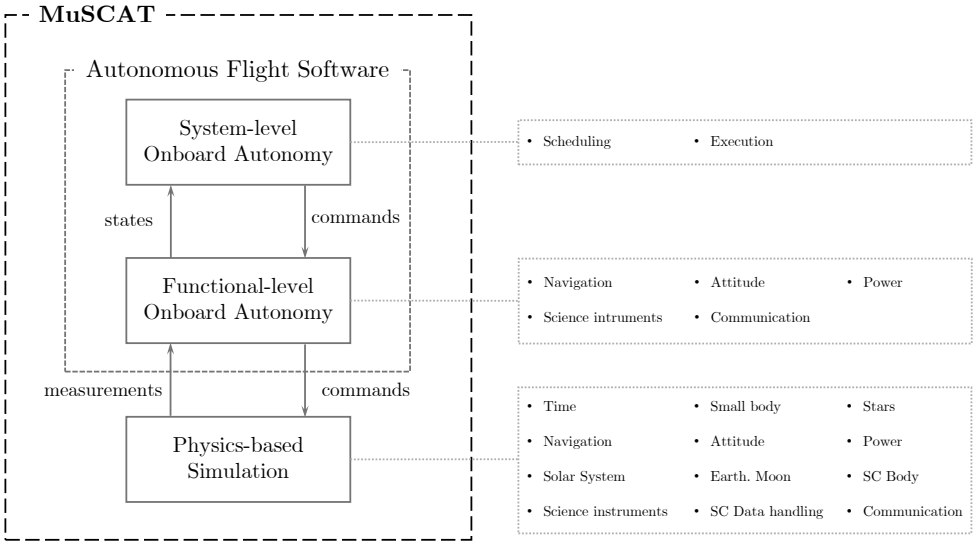

Figure 3: Components of the Multi-Spacecraft Concept and Autonomy Tool (MuSCAT).[32]

outputs observed states to the system layer, which, in turn, sends commands back to the functional layer. In this work, the navigation and attitude determination and control subsystems were enhanced and fully integrated.

Physics-based Simulation The Physics-based Simulation layer contains all the data and functions needed to execute the simulation. It monitors onboard time, planetary bodies, and spacecraft subsystems.

In the following sections, the mathematical foundations of the algorithms implemented in MuSCAT will be described, and the results for each algorithm will be presented based on a 20-day simulation at an orbital distance of 5 times the radius of (99942) Apophis, without considering any thrust error.

Attitude estimation

Spacecraft attitude estimation determines the orientation of the spacecraft relative to a reference frame. It is of paramount importance for performing scientific operations, ensuring precise navigation and control, managing power, and exchanging data. Attitude estimation is carried out using sensors such as star trackers, sun sensors, and IMU. The primary assumption made in this work is that the spacecraft behaves as a rigid body. This implies that the spacecraft dynamics are modeled without considering any deformations or structural vibrations that might occur.

Equations of motion The attitude of the spacecraft, described as a quaternion, is usually propagated using the continuous time spacecraft kinematic equation

$$\dot{\mathbf{q}}(t) = \frac{1}{2}\Xi(\mathbf{q}(t))\omega(t) = \frac{1}{2}\Omega(\omega(t))\mathbf{q}(t) = \frac{1}{2}\begin{bmatrix}\omega(t)\\0\end{bmatrix} \otimes \mathbf{q}(t) \tag{2}$$

Where $\omega(t)$ is the continuous time spacecraft angular rate and $\mathbf{q}$ is the spacecraft attitude quaternion, defined by a vectorial $\bar{v}$, and a scalar s part.

$$\mathbf{q} = \begin{bmatrix} \bar{v} \\ s \end{bmatrix}; \quad \bar{v} \in \mathbb{R}^3; \quad s \in \mathbb{R}^1 \tag{3}$$

$$\Xi(\mathbf{q}) = \begin{bmatrix} sI_{3\times 3} + \bar{v}^{\times} \\ -\bar{v}^T \end{bmatrix}; \quad \Omega(\omega) = \begin{bmatrix} -\omega^{\times} & \omega \\ -\omega^T & 0 \end{bmatrix} \tag{4}$$

where $[.]^{\times}$ is the skew or cross-product matrix. The kinematic equation is usually coupled with the dynamics equation to retrive the spacecraft angular rate.

$$J\dot{\omega}(t) = J\omega(t) \times \omega(t) + \tau(t) \tag{5}$$

where J is the spacecraft inertia matrix, ω represents the angular velocity, and τ the external torques. The primary issue with this dynamics equation, especially for miniaturized platforms such as CubeSats, is that the angular velocity values can be extremely small, leading to numerical propagation issues. To address this, in this work, the dynamics equation is not considered, and the IMU measurements, which are typically present on spacecraft, are used in the propagation step rather than in the update step. Since the IMU measurements directly influence the kinematic equations, it is necessary to also estimate the constant bias arising from the IMU hardware. Consequently, the state vector for the filter implementation is a 7-dimensional vector, comprising the quaternion vector $\boldsymbol{q}$ and the IMU bias $\boldsymbol{b}$.

$$\mathbf{x}(t) = \begin{bmatrix} \mathbf{q}(t) \\ \mathbf{b}(t) \end{bmatrix} \tag{6}$$

Since angular velocity is measured discretely by the IMU, it is necessary to quantify the discrete-time evolution of both the biases and the quaternions. While the bias drift is assumed to evolve according to the discrete-time Equation 12, computing the discrete-time evolution of the quaternions requires some assumptions:

- Small estimation time step Δt_k
- Constant angular velocity over the time step

Both assumptions are valid owing to the high update frequency of the IMU, which is considered around $10\,\mathrm{Hz}$.

Since Equation 2 is in the form $\dot{\boldsymbol{x}}(t) = A\boldsymbol{x}(t) + \boldsymbol{b}$, where $\boldsymbol{q}(t) = \boldsymbol{x}(t)$, $A = \frac{1}{2}\Omega(\boldsymbol{\omega}(t))$ and $\boldsymbol{b} = \mathbf{0}$.
The equation can be easily discretized, leading to

$$\boldsymbol{q}(t + \Delta t) = \left[I + \frac{1}{2}\Omega(\boldsymbol{\omega}(t)\Delta t) \right] \boldsymbol{q}(t) \tag{7}$$

which is equivalent to

$$\boldsymbol{q}_k = \boldsymbol{q}(\boldsymbol{\omega}_{k-1}\Delta t_k) \otimes \boldsymbol{q}_{k-1} \tag{8}$$

The quantity $\boldsymbol{\omega}_k \Delta t_k$ represents a small rotation $\boldsymbol{\theta}$. For this reason, the quaternion $\boldsymbol{q}$ can be represented as:

$$\boldsymbol{q}(\boldsymbol{\theta}) = \begin{bmatrix} \sin\frac{\theta}{2}\frac{\boldsymbol{\theta}}{\theta} \\ \cos\frac{\theta}{2} \end{bmatrix} \approx \begin{bmatrix} \frac{\boldsymbol{\theta}}{2} \\ 1 \end{bmatrix} \tag{9}$$

Combining the quaternion and bias time evolution, it is possible to write the dicrete-time, nonlinear equation of the system:

$$\boldsymbol{x}_k = \begin{bmatrix} \boldsymbol{q}_k \\ \boldsymbol{b}_k \end{bmatrix} = \begin{bmatrix} \boldsymbol{q}(\boldsymbol{\omega}_{m,k-1}\Delta t_k) \otimes \boldsymbol{q}_{k-1} \\ \boldsymbol{b}_{k-1} + \sigma_u \end{bmatrix} = g(\boldsymbol{x}_{k-1}, \boldsymbol{\omega}_{m,k-1}, \sigma_{k-1}) \tag{10}$$

where $g(\boldsymbol{x}_{k-1}, \boldsymbol{\omega}_{m,k}, \sigma_{k-1})$ represents the nonlinear dynamics as a function of the state at the previous time $\boldsymbol{x}_{k-1}$, the measured angular velocity $\boldsymbol{\omega}_{m,k-1}$, and the process noise σ_{k-1}.

Sensors In this section, the main sensors considered in this work are described and modeled.

IMU model. The measurements from the IMU provide the angular rate of the spacecraft along its three axes. It is assumed that the gyroscope is affected only by zero-mean white Gaussian noise and a bias modeled as a first-order random walk. The measured angular velocity of the spacecraft at time t_k is represented as:[33,34]

$$\boldsymbol{\omega}_{m,k} = \boldsymbol{\omega}_k + \boldsymbol{b}_k + \sigma_v \tag{11}$$

where $\boldsymbol{\omega}_{m,k}$ denotes the measured angular velocity, $\boldsymbol{\omega}_k$ is the true angular velocity of the spacecraft, $\boldsymbol{b}_k$ is the bias, and σ_v stands for a zero-mean, Gaussian white-noise sequence with covariance $Q_{1,k}$. The walking bias is assumed to evolve following a first-order random walk:

$$\boldsymbol{b}_k = \boldsymbol{b}_{k-1} + \sigma_u \tag{12}$$

where σ_u is a zero-mean, Gaussian white-noise of covariance $Q_{2,k}$.
Substituting everything in Equation 11, we get the true angular velocity in terms of the gyroscope bias and process noise.

$$\boldsymbol{\omega}_k = \boldsymbol{\omega}_{m,k} - \boldsymbol{b}_{k-1} - \sigma_v - \sigma_u \tag{13}$$

The expected value of the true angular velocity $\hat{\boldsymbol{\omega}}_k$ is therefore given by

$$\hat{\boldsymbol{\omega}}_k = \boldsymbol{\omega}_{m,k} - \hat{\boldsymbol{b}}_{k-1} \tag{14}$$

The covariance values $Q_{1,k}$ and $Q_{2,k}$ can be computed from the considered IMU specifications as follows.

$$Q_{1,k} = \left[\frac{ARW\frac{\text{deg}}{\sqrt{\text{s}}}}{\sqrt{\Delta t_k}}\right]^2 I_3 = \left[\frac{2.62 \times 10^{-5}}{\sqrt{0.1}}\right]^2 I_3 \tag{15}$$

$$Q_{2,k} = \left[GBI\frac{\text{deg}}{\text{s}}\right]^2 I_3 = \left[1.07 \times 10^{-5}\right]^2 I_3 \tag{16}$$

where Δt_k is the IMU sampling time, ARW is the gyro Angular Random Walk, and GBI is the Gyro Bias Instability.

Attitude sensors model. In this study, it is assumed that attitude sensors are capable of directly measuring orientation in terms of quaternions, which are subject to measurement errors. Due to the nature of quaternions as unit vectors, it is not feasible to simply add white Gaussian noise to the true quaternion, as is done for IMU measurements. Therefore, to simulate the measurement errors arising from the star tracker and sun sensor, the true quaternion is rotated by a perturbation quaternion vector.

$$\boldsymbol{z}_k = \begin{bmatrix} \frac{1}{2}\boldsymbol{v}_k \\ 1 \end{bmatrix} \otimes \boldsymbol{q}_k \tag{17}$$

Where $\otimes$ represents the quaternion multiplication, $\boldsymbol{z}_k$ is the quaternion measurement, and $\boldsymbol{v}_k$ is a measurement noise expressed as a rotation vector with standard deviation σ_{STA} and σ_{SS}, for the star tracker and the sun sensor, respectively. The rotation perturbation is assumed small such that this measurement model is valid. The measurement covariance matrix R_{AE} can be defined as

$$R_{AE} = \sigma_{STA}^2 I_3 \tag{18}$$

The matrix can be defined equivalently for the sun sensor substituting σ_{STA} with σ_{SS}.
Table 4 reports all the numerical values used in simulations to model the spacecraft sensors.

Table 4: Relevant parameters for sensor modeling

ARW [deg/$\sqrt{\text{s}}$]	GBI [deg/s]	Δt_k [s]	σ_{STA} [deg]	σ_{SS} [deg]
2.62×10^{-5}	1×10^{-6}	0.1	0.01	0.5

Prediction step of EKF The temporal evolution of the estimated state vector is given by Equation 10 without process noises:

$$\hat{\boldsymbol{x}}_k = \begin{bmatrix} \hat{\boldsymbol{q}}_k \\ \hat{\boldsymbol{b}}_k \end{bmatrix} = \begin{bmatrix} \boldsymbol{q}(\hat{\boldsymbol{\omega}}_{m,k}\Delta t_k) \otimes \boldsymbol{q}_{k-1} \\ \boldsymbol{b}_{k-1} \end{bmatrix} = g(\hat{\boldsymbol{x}}_{k-1}, \hat{\boldsymbol{\omega}}_{m,k}) \tag{19}$$

While the covariance matrix P can be comupted as

$$P_{\text{AE},k} = F_{\text{AE}} P_{\text{AE},k-1} F_{\text{AE}}^T + Q_{\text{AE}} \tag{20}$$

where the matrices F_{AE} and Q_{AE} are[35]

$$F_{\text{AE}} = e^{F_c \Delta t_k} \quad \text{where} \quad F_c = \begin{bmatrix} -\hat{\omega}(t)^\times & -I_3 \\ 0_3 & 0_3 \end{bmatrix} \tag{21}$$

$$Q_{\text{AE}} = \begin{bmatrix} \left(\sigma_v^2 \Delta t_k + \frac{1}{3}\sigma_u^2 \Delta t_k^3\right) I_3 & -\left(\frac{1}{2}\sigma_u^2 \Delta t_k^2\right) I_3 \\ -\left(\frac{1}{2}\sigma_u^2 \delta t_k^2\right) I_3 & \left(\sigma_u^2 \Delta t_k\right) I_3 \end{bmatrix} \tag{22}$$

Update step of EKF To correct the attitude considering the measurements coming from the sensors, the residual between the estimated attitude $\hat{\mathbf{q}}_k$ and the measurement $\mathbf{z}_k$ is computed

$$\Delta \boldsymbol{z}_{q,k} = \boldsymbol{z}_k \otimes \hat{\boldsymbol{q}}_k^c = \begin{bmatrix} \frac{1}{2}\boldsymbol{v}_k \\ 1 \end{bmatrix} \otimes \boldsymbol{q}_k \otimes \hat{\boldsymbol{q}}_k^c = \begin{bmatrix} \frac{1}{2}\boldsymbol{v}_k \\ 1 \end{bmatrix} \otimes \delta \boldsymbol{q}_k \tag{23}$$

where $\mathbf{q}^{\mathbf{c}}$ represents the quaternion conjugate. Because both the attitude error and the measurement noise are assumed small, second-order terms can be neglected and we can consider only the vectorial part.

$$\Delta \boldsymbol{z}_{q,k} = \delta \boldsymbol{q}_k + \frac{1}{2}\boldsymbol{v}_k \tag{24}$$

This quaternion representation of the attitude residual can be expressed in terms of a rotation vector through Equation 9 to get a measurement model in the form typically used by the Kalman filter

$$\Delta \boldsymbol{z}_k = \delta \boldsymbol{\theta}_k + \boldsymbol{v}_k = H_{\mathrm{AE},k}\delta \boldsymbol{x}_k + \boldsymbol{v}_k \tag{25}$$

The $H_{\mathrm{AE},k}$ matrix can assume multiple forms depending on the sensors onboard the spacecraft. For a single sensor

$$H_{\mathrm{AE},k} = [I_3 \quad 0_3] \tag{26}$$

while the $\boldsymbol{v}_k$ depends on the noise of the sensor itself. The update step of the filter is computed as:

$$S_{\mathrm{AE},k} = H_{\mathrm{AE},k} P_{\mathrm{AE},k} H_{\mathrm{AE},k}^T + R_{\mathrm{AE},k} \tag{27}$$

$$K_{\mathrm{AE},k} = P_{\mathrm{AE},k} H_{\mathrm{AE},k}^T S_{\mathrm{AE},k}^{-1} \tag{28}$$

$$\Delta \boldsymbol{x}_k = \begin{bmatrix} \Delta \boldsymbol{\theta}_k \\ \Delta \mathbf{b}_k \end{bmatrix} = K_{\mathrm{AE},k} \Delta \boldsymbol{z_k} \tag{29}$$

$$P_{\mathrm{AE},k}^+ = [I - K_{\mathrm{AE},k} H_{\mathrm{AE},k}] P_{\mathrm{AE},k}^- \tag{30}$$

$$\hat{\boldsymbol{q}}_k^+ = \begin{bmatrix} \sin \frac{||\Delta \boldsymbol{\theta}_k||}{2} \frac{\Delta \boldsymbol{\theta}_k}{||\Delta \boldsymbol{\theta}_k||} \\ \cos \frac{||\Delta \boldsymbol{\theta}_k||}{2} \end{bmatrix} \otimes \hat{\boldsymbol{q}}_k^- \tag{31}$$

$$\hat{\boldsymbol{b}}_k^+ = \hat{\boldsymbol{b}}_k^- + \Delta \boldsymbol{b}_k \tag{32}$$

Figures 4, 5, and 6 show the orientation along with the covariance bounds, the bias, and the angular velocity error profiles, over the first $90\ \mathrm{min}$ of the simulation. Only the initial minutes are displayed for visualization purposes. From these figures, it can be observed that within a few seconds, the filter accurately estimates both the spacecraft attitude and the IMU biases. Moreover, the attitude error shown in Figure 4 consistently remains within the 3σ bounds of the covariance matrix. The increase in covariance around $1000\ \mathrm{s}$ is due to a slew maneuver occurring at that time, during which no estimation is performed. The same applies to the angular velocity, which remains below 2×10^{-4} $\mathrm{deg/s}$ except during slew maneuvers.

Attitude control

The final goal of attitude control is to stabilize a spacecraft in the presence of various errors, including uncertain physical parameters, disturbances, sensor measurement inaccuracies, and actuator saturation.

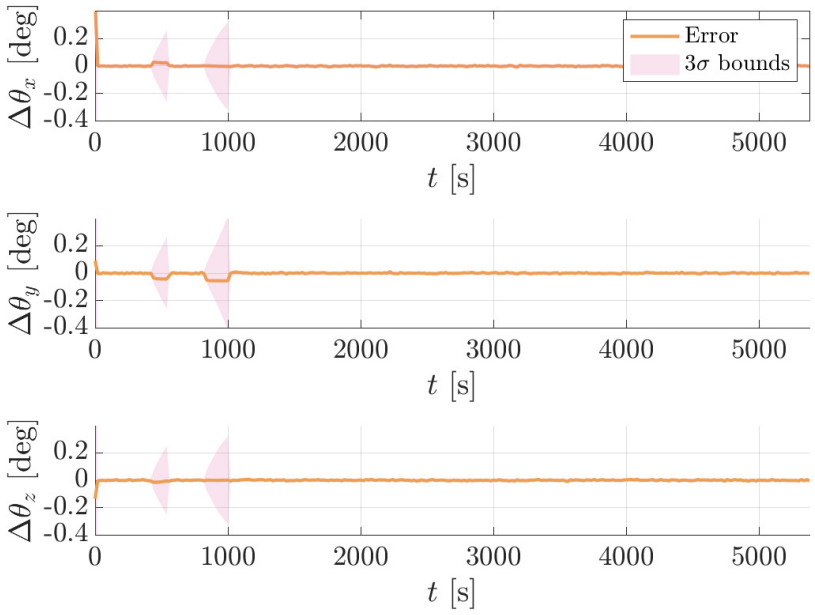

Figure 4: Attitude error profile with covariance bounds.

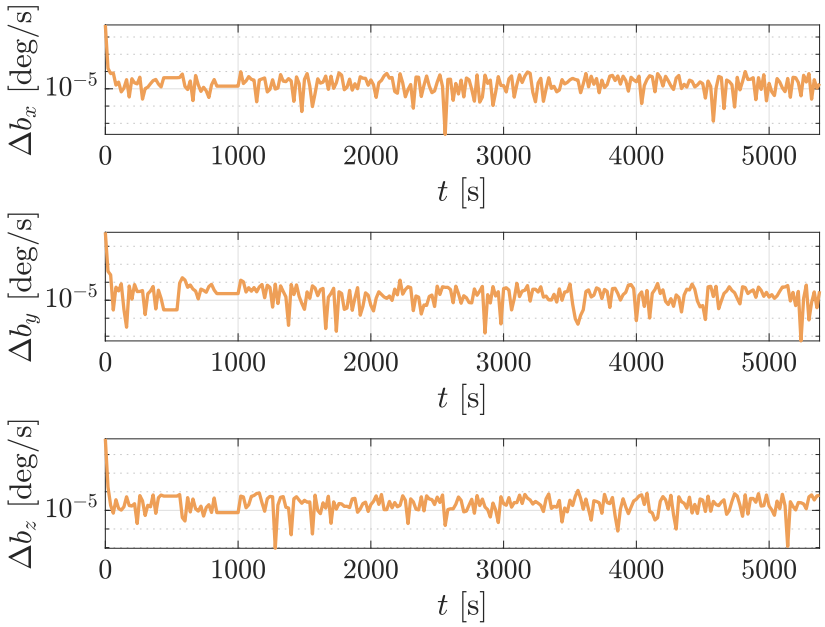

Figure 5: Biases estimation error.

System attitude stabilization involves controlling the evolution of angular velocity during the attitude transient and achieving a desired final attitude at steady state. This can be summarized by

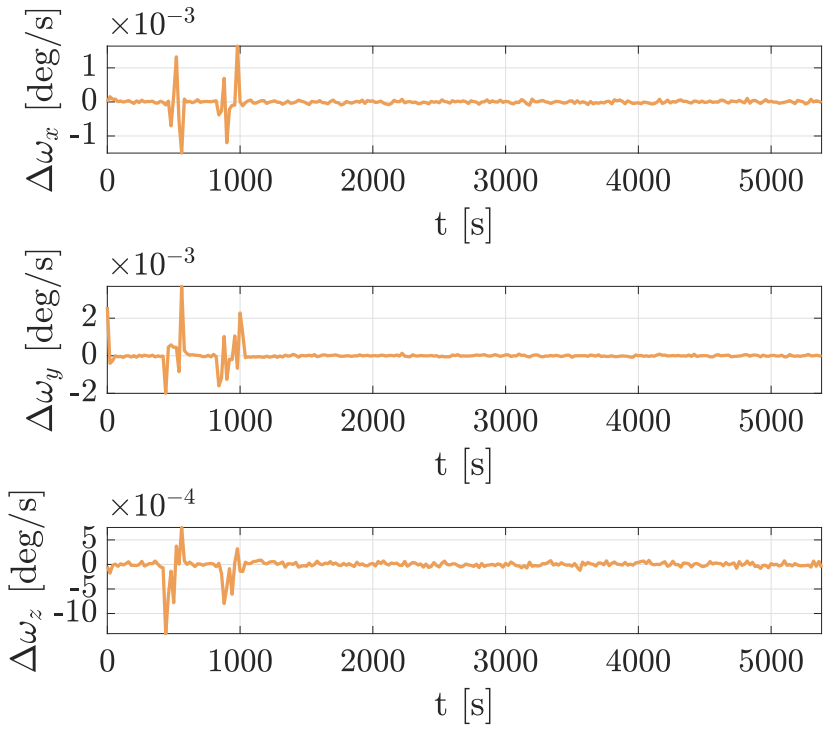

Figure 6: Angular velocity estimation error.

specifying two conditions

$$||\omega(t)||_2 \leq \epsilon_{trans} \quad \forall t > 0 \tag{33}$$

$$\mathbf{q}(t) \otimes \mathbf{q}_f^c \leq \epsilon_{ss} \quad \forall t > T \tag{34}$$

where ϵ_{trans} is the transient error bound, selected to ensure that the system remains within the technological capabilities of the sensors and actuators onboard the spacecraft. While ϵ_{ss} represents the steady-state angular error bound that the system has to keep when the final desired attitude $\mathbf{q}_f$ is achieved after the steady-state time T, with $T >> 0$, the value of which depends on the desired attitude mode.

A robust nonlinear attitude tracking control law has been considered to address the previously stated problem. The control law, thoroughly defined by Bandyopadhyay,[36] computes the desired control $\mathbf{u}_c$ based on the desired attitude trajectory $\mathbf{q}_{d,k}$, and the positive-definite constant gain matrices $\mathbf{K}_r \in \mathbb{R}^{3\times3}$ and $\mathbf{\Lambda}_r \in \mathbb{R}^{3\times3}$.

$$\mathbf{u}_c = -\mathbf{K}_r(\hat{\omega}_k - \omega_{r,k}) \tag{35}$$

where

$$\omega_{r,k} = \omega_{d,k} + \frac{1}{2}\mathbf{Z}(\hat{\mathbf{q}}_k)^+ \mathbf{\Lambda}_r(\mathbf{q}_{d,k} - \hat{\mathbf{q}}_k) \tag{36}$$

and

$$\mathbf{Z}(\hat{\mathbf{q}}) = \begin{bmatrix} \hat{s}I_3 + \hat{v}^\times \\ \hat{v}^T \end{bmatrix} \tag{37}$$

This robust nonlinear tracking control law guarantees globally exponential convergence of the system attitude to the desired attitude trajectory. Table 5 shows all the relevant parameters used in simulations.
Figure 7 shows the control, profiled, and knowledge errors for the first two days of the simulation. The control error θ_{ctrl}, represents the angular separation between the estimated attitude and the profiled one. Peaks of $5\ \mathrm{deg}$ are reached because, beyond that value, a slew maneuver is performed. The profiled error θ_{prof}, is the angle between the commanded and profiled attitudes, and it can reach a maximum value of $180\ \mathrm{deg}$. Finally, the knowledge error θ_{knl}, represents the angular separation between the estimated and true attitudes. It never exceeds $0.2\ \mathrm{deg}$, indicating that the attitude control is functioning correctly throughout the simulation.
The selection of the actuator to use is driven by two conditions

$$\theta_{ctrl} > 11.46\ \mathrm{deg} \tag{38}$$

$$\hat{\omega} > 0.17\ \mathrm{deg/s} \tag{39}$$

When at least one of these conditions is satisfied, micro-thrusters are employed for attitude control, otherwise, reaction wheels are used. The only scenario in which micro-thrusters are used when neither condition is met is when the reaction wheels saturate, specifically when they reach 80% of their maximum velocity. Figure 8a shows the angular velocity evolution of the reaction wheels throughout the simulation for attitude control, while Figure 8b shows the torque profile of the micro-thrusters. It is clear that the micro-thrusters are employed only when reaction wheels saturation occurs.

Table 5: Relevant parameters for attitude control

ϵ_{trans} [deg/s]	ϵ_{ss} [deg]	$\mathbf{K}_r$ $[-]$	$\mathbf{\Lambda}_r$ $[-]$
1	5	$0.02I_3$	$0.01I_3$

Orbital estimation

To enable spacecraft autonomous navigation, vision-based navigation algorithms that use the onboard camera to acquire images of the asteroid are among the most promising techniques. These images are used to detect surface landmarks, which are N_{lmk} salient surface points identified by a mothercraft during earlier mission phases. Each landmark detected in an image can be treated as a line-of-sight measurement, representing the direction from the spacecraft to the landmark. By processing multiple line-of-sights simultaneously, it is possible to estimate the spacecraft trajectory. In this work, the camera line-of-sight measurements have been simulated using a pinhole camera model. The main assumption of this work is an ideal knowledge of the spacecraft attitude state. There is no propagation of uncertainties and planning of measurement acquisitions, as is typically done in ground control space missions.

Measurement model The assumption of a pinhole camera model implies that a 3D point in the scene is perfectly projected onto the 2D camera plane, with the projection perturbed by a zero-mean Gaussian noise ν to account for error sources such as lens distortions, noise, calibration errors, and inaccuracies in landmark position knowledge. Consequently, the position of a 3D landmark $\mathbf{l}$ relative to the asteroid center of mass is represented by its pixel location $\mathbf{y} = [u \quad v]^T$ within the

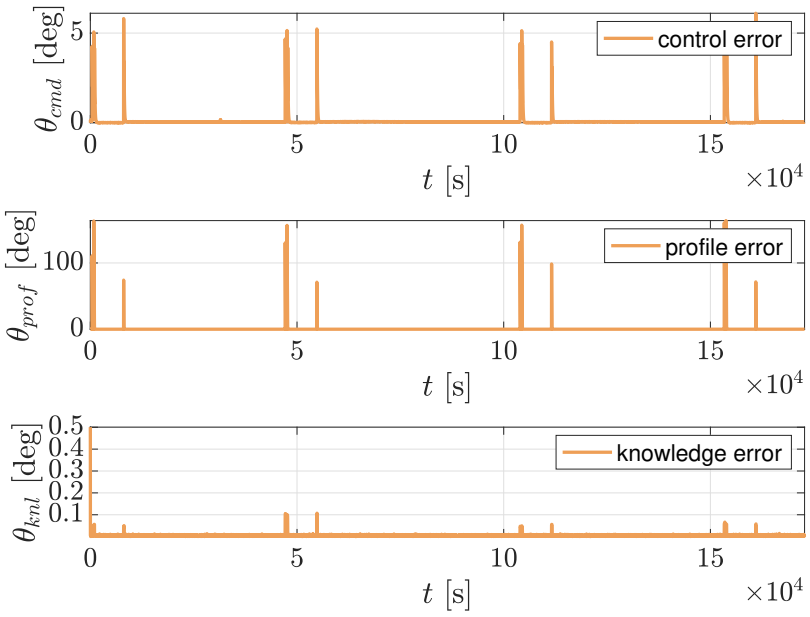

Figure 7: Control, profiled, and knowledge errors.

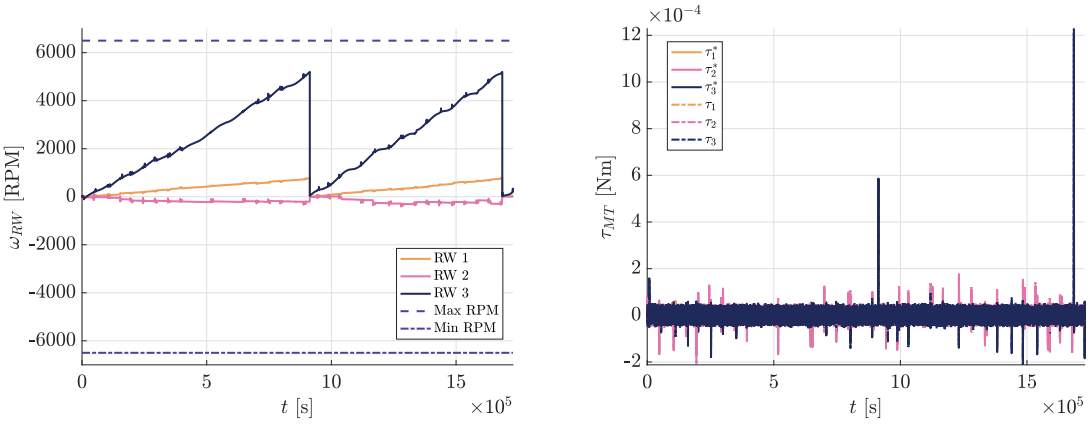

(a) (b)

Figure 8: Reaction wheels angular velocity evolution (a) and micro-thrusters torque profile (b).

image. This measurement is modeled as

$$u = f\frac{(\mathbf{l}-\mathbf{r})^T \cdot \hat{\mathbf{j}}_c}{(\mathbf{l}-\mathbf{r})^T \cdot \hat{\mathbf{i}}_c} + u_0 + \nu_u \tag{40}$$

$$v = f\frac{(\mathbf{l}-\mathbf{r})^T \cdot \hat{\mathbf{k}}_c}{(\mathbf{l}-\mathbf{r})^T \cdot \hat{\mathbf{i}}_c} + v_0 + \nu_v \tag{41}$$

where f is the camera focal length, u_0 and v_0 are the half-dimensions of the sensor, expressed in units of pixels, and $\hat{\mathbf{i}}_c$, $\hat{\mathbf{j}}_c$, and $\hat{\mathbf{k}}_c$ are the unit vectors of the spacecraft body fixed frame. Among all the landmarks, only those within the camera Field of View (FoV), not shaded by the surface of the body (assumed to be spherical), and illuminated by sunlight, can be detected.
The measurement covariance matrix R_{OD} can be defined as

$$R_{\text{OD}} = \begin{bmatrix} \nu_u^2 & 0 \\ 0 & \nu_v^2 \end{bmatrix} \tag{42}$$

The spacecraft considered in this work has the camera normal vector aligned with the $\hat{\mathbf{i}}_c$ axis of the spacecraft. If a different spacecraft configuration is considered, the orbital estimation equations must be adjusted accordingly.

Dynamics The state estimation problem aims to determine the spacecraft state $\mathbf{x}$ in terms of position and velocity relative to the asteroid center of mass in the inertial frame.

$$\mathbf{x} = [\mathbf{r} \quad \dot{\mathbf{r}}]^T = [x \quad y \quad z \quad \dot{x} \quad \dot{y} \quad \dot{z}]^T \tag{43}$$

where $\mathbf{r} = [x \quad y \quad z]^T$ and $\dot{\mathbf{r}} = [\dot{x} \quad \dot{y} \quad \dot{z}]^T$ are the spacecraft position and velocity vectors relative to the inertial frame centered in the asteroid center of mass. The objective is to estimate the state evolution over time as well as its associated covariance using landmark-based observations.
During asteroid close proximity operations, three main accelerations significantly impact the spacecraft dynamics, namely the asteroid gravity field, the SRP, and the control accelerations generated by thrusters. The nonlinear spacecraft dynamics can be formulated as

$$\ddot{\mathbf{r}} = \mathbf{a}_b + \mathbf{a}_{\text{SRP}} + \mathbf{a}_{\text{u}} \tag{44}$$

where $\mathbf{a}_b$, $\mathbf{a}_{\text{SRP}}$, and $\mathbf{a}_{\text{u}}$ are the acceleration caused by the main body, the SRP, and the control actions, respectively.
The acceleration induced by the main body is modeled using a spherical harmonics expansion up to the 8^{th} order. The spacecraft position and velocity are propagated using the `ode113` MATLAB integrator, and every Δt_{msr}, if a measurement is available, the state is corrected. During propagation, the state transition matrix Φ is also updated. This matrix maps the evolution of the initial state error and is used for propagating the covariance matrix.
The state covariance matrix $Q_{\text{OD},k}$ is also defined as

$$Q_{\text{OD},k} = \sigma_w^2 \begin{bmatrix} \frac{\Delta t_k^3}{3} I_3 & \frac{\Delta t_k^2}{2} I_3 \\ \frac{\Delta t_k^2}{2} I_3 & \Delta t_k \end{bmatrix} \tag{45}$$

where σ_w represent the standard deviation for random unmodeled accelerations. The covariance matrix is then computed as

$$P_{\text{OD},k} = \Phi_k P_{\text{OD},k-1} \Phi_k^T + Q_{\text{OD},k} \tag{46}$$

When landmark measurements are available, they are processed individually and the H matrix is evaluated.

$$H_{\text{OD}} = \begin{bmatrix} \frac{\partial u}{\partial r}^T & 0 & 0 & 0 \\ \frac{\partial v}{\partial r}^T & 0 & 0 & 0 \end{bmatrix} \tag{47}$$

where

$$\frac{\partial u}{\partial r} = f\frac{-\hat{\mathbf{j}}_c[(\mathbf{l}-\mathbf{r})^T\hat{\mathbf{i}}_c] + \hat{\mathbf{i}}_c[(\mathbf{l}-\mathbf{r})^T\hat{\mathbf{j}}_c]}{[(\mathbf{l}-\mathbf{r})^T\hat{\mathbf{i}}_c]^2} \tag{48}$$

$$\frac{\partial v}{\partial r} = f\frac{-\hat{\mathbf{k}}_c[(\mathbf{l}-\mathbf{r})^T\hat{\mathbf{i}}_c] + \hat{\mathbf{i}}_c[(\mathbf{l}-\mathbf{r})^T\hat{\mathbf{k}}_c]}{[(\mathbf{l}-\mathbf{r})^T\hat{\mathbf{i}}_c]^2} \tag{49}$$

The residual between the estimated and the measured pixel location is computed

$$\Delta\mathbf{y}_k = \mathbf{y}_k - \hat{\mathbf{y}}_k \tag{50}$$

Finally, the update step of the filter is computed as:

$$S_{\text{OD},k} = H_{\text{OD},k}P_{\text{OD},k}H_{\text{OD},k}^T + R_{\text{OD},k} \tag{51}$$

$$K_{\text{OD},k} = P_{\text{OD},k}H_{\text{OD},k}^T S_{\text{OD},k}^{-1} \tag{52}$$

$$\boldsymbol{x}_k^+ = \boldsymbol{x}_k^- + K_{\text{OD},k}\Delta\boldsymbol{y}_k \tag{53}$$

$$P_{\text{OD},k}^+ = [I_6 - K_{\text{OD},k}H_{\text{OD},k}]P_{\text{OD},k}^-[I_6 - K_{\text{OD},k}H_{\text{OD},k}]^T + K_{\text{OD},k}R_{\text{OD},k}K_{\text{OD},k}^T \tag{54}$$

In Table 6, all the relevant parameters for orbit determination are reported.

Figures 9 and 10 show the position and velocity estimation error profiles, along with the covariance bounds throughout the whole simulation. It can be observed the filter accurately estimates both position and velocity, wheres errors consistently remain within the 3σ bounds of the covariance matrix. The increase in covariance is due to the fact that the spacecraft is not pointing towards the asteroid, and consequently it is not able to acquire images of it and perform orbit determination.

Table 6: Relevant parameters for orbit determination

f [pxl]	FOV [deg]	$[u_0, v_0]$ [pxl]	σ_z [pxl]	σ_w [km/s^2]	Δt_{msr} [s]	N_{lmk} [$-$]
1.1×10^3	50	$[512, 512]$	0.25	1×10^{-9}	600	20

Synthetic image generation To enhance the orbit determination pipeline, an algorithm for the synthetic generation of realistic images of minor bodies has also been integrated into MuSCAT. This capability is highly valuable for future applications involving more sophisticated software-in-the-loop, vision-based methods for autonomous orbit determination. In this work, the optical measurements are simulated, bypassing the image processing step that is inherently embedded in an optical navigation pipeline.

The starting point for image generation is a high-resolution, three-dimensional model of the asteroid. Most models available online are generated through light-curve analysis; therefore, they lack morphological features such as surface roughness and boulders. These features are procedurally generated on the surface of the body. First, Fractional Brownian Motion (FBM) noise is used to perturb the vertices of the mesh along their normals. Multiple layers (or octaves) of noise are generated at various scales to create a fractal-like surface typical of rocky terrains.

Next, a library of rocks is generated. The base shape of each rock is an icosahedron* whose triangular mesh is refined recursively. These basic shapes are then perturbed using a combination of ellipsoidal deformations, which randomly stretch and compress the original boulders, and FBM

*A polyhedron with 20 equilateral triangular faces

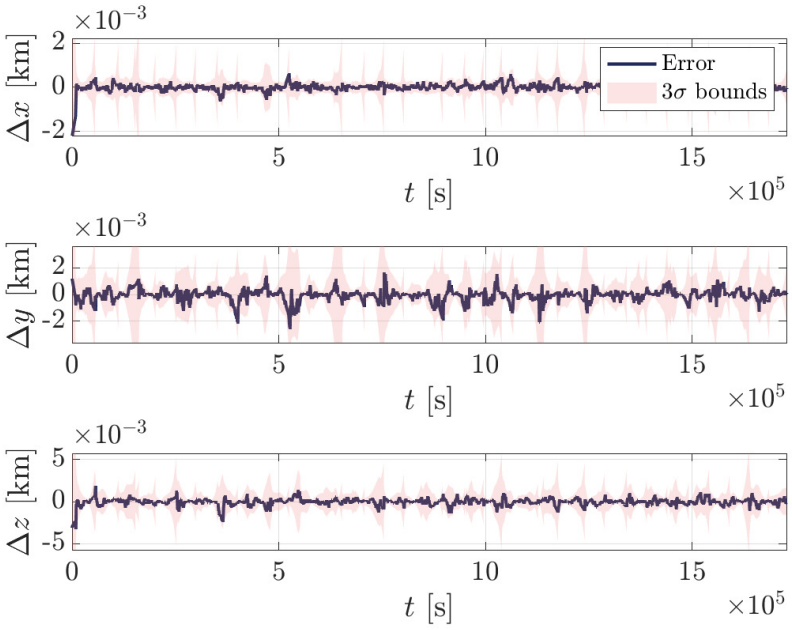

Figure 9: Position error profile with covariance bounds.

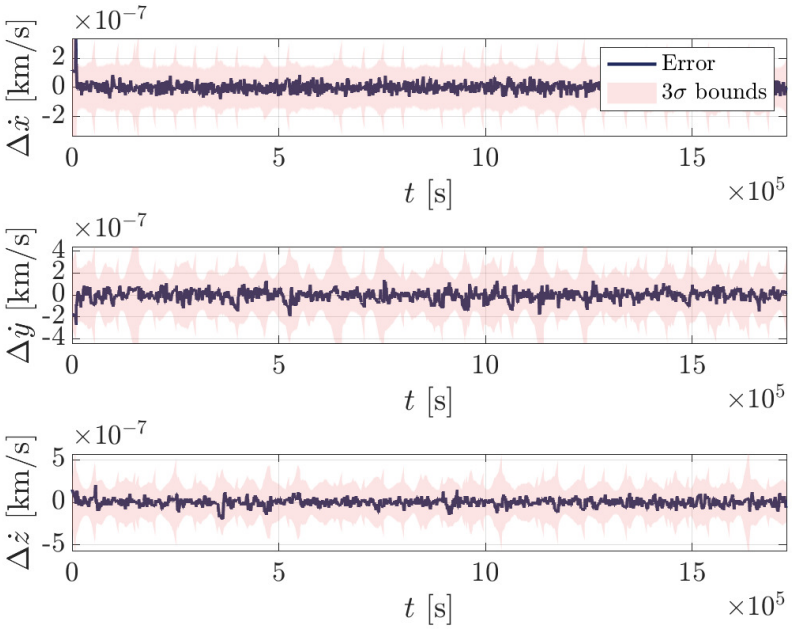

Figure 10: Velocity error profile with covariance bounds.

noise. This approach allows for the creation of randomized and realistic rock shapes. The next step involves placing the boulders on the mesh surface. The rocks are first randomly rotated to en-

sure that each rock appears unique in orientation and then placed on eligible mesh facets, avoiding overlapping and unnatural placements. Each boulder is assigned a different base color to allow the asteroid albedo to vary.
Once the final mesh is built, the lighting conditions of each facet are computed based on the Sun direction (assumed to be collimated light at infinity) and the observer position. The Hapke shading model is then employed to recreate realistic lighting conditions. In Figure 11, three synthetic images generated in MuSCAT are shown.

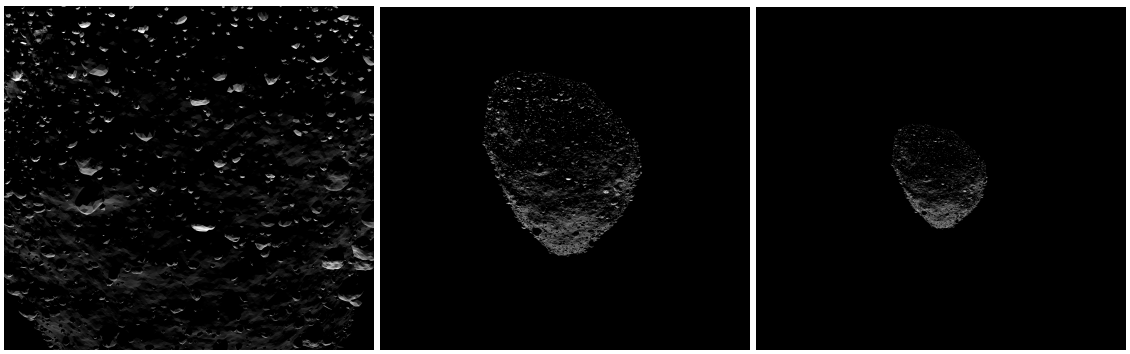

(a) (b) (c)

Figure 11: Images synthetically generated in MuSCAT. From left to right, images taken at 2 d_{SC-SB} (a), 5.5 d_{SC-SB} (b), and 9 d_{SC-SB} (c).

Orbital control

Lambert's problem involves determining the orbit of a body that moves from one position to another in a specified time interval. Given two position vectors $\mathbf{r}_1$ and $\mathbf{r}_2$ at times t_1 and t_2, respectively, along with the time of flight $\Delta t_{TCM} = t_2 - t_1$, the goal is to find the initial and final velocity vectors v_1 and v_2 that allow the body to move from r_1 to r_2 in the given time. The traditional Lambert problem is solved when the body is under the influence of a central gravitational field governed by the two-body equations of motion. In case of close proximity operations to asteroids, this assumption fails as the gravitational field is highly non-linear and strong perturbations such as the SRP are present.

When some prescribed thresholds are exceeded, in this case the distance from the nominal trajectory, the on-board computer promptly triggers a TCM. The first step is to compute the position $\mathbf{r}_1$ where the spacecraft needs to execute the position control burn. This position is determined by propagating the trajectory for 200 s, which is the maximum time (with a margin) needed for the spacecraft to adjust from its current attitude to the desired one (chemical thruster aligned with the $\Delta\mathbf{v}_1$ direction). The final desired position on the nominal trajectory, $\mathbf{r}_2$, is computed by considering the position on the nominal trajectory at a prescribed time interval Δt_{TCM} from t_1. In this work, it is assumed that the separation between the position and velocity control burns is set to a constant value. Once the times and positions are determined, the Lambert-Battin algorithm[37] is employed to compute the control maneuvers $\Delta\mathbf{v}_1$ and $\Delta\mathbf{v}_2$, which are then translated into an impulse from the onboard chemical thruster. The desired thrust T is computed using the following equation

$$T = \frac{(\Delta V - \Delta V_{\text{executed}})m}{\Delta t_{\text{sim}}} \tag{55}$$

where m is the spacecraft mass, $\Delta V_{\text{executed}}$ is the already executed maneuver, and Δt_{sim} is the simulation time step. The term $\Delta V_{\text{executed}}$, initially set to 0, is introduced because it can be possible that the thrust needed in the simulation time step exceeds the maximum thrust capability of the CubeSat. In such cases, the maneuver is spreaded over time until $\Delta V - \Delta V_{\text{executed}}$ goes to zero. Note also that the minimum allowable thrust is set to 0, meaning that even the smallest maneuver can be achieved by the thruster.
The simplified equations of motion for achieving orbital control are described by

$$\ddot{\mathbf{r}} = -\mu \frac{\mathbf{r}}{r^3} + \mathbf{a}_{\text{pert}}, \tag{56}$$

and are numerically propagated using the `ode113` MATLAB integrator. This control does not account for uncertainties in the gravitational field; instead, it assumes a point mass model, resulting in a control that is not ideal due to the difference between the true and the modeled dynamics.
Figure 12a shows the desired, true, and estimated distances from (99942) Apophis. The three curves nearly overlap perfectly, indicating that both orbital determination and control are functioning correctly. The oscillation in the orbital distance is caused by the SRP, which perturbs the spacecraft trajectory. Figure 12b shows the thrust profile evolution throughout the simulation. The thrust exceeds 0.2 N in the initial steps due to the spacecraft initial dispersion, but it then stabilizes with TCMs below 0.1 N.

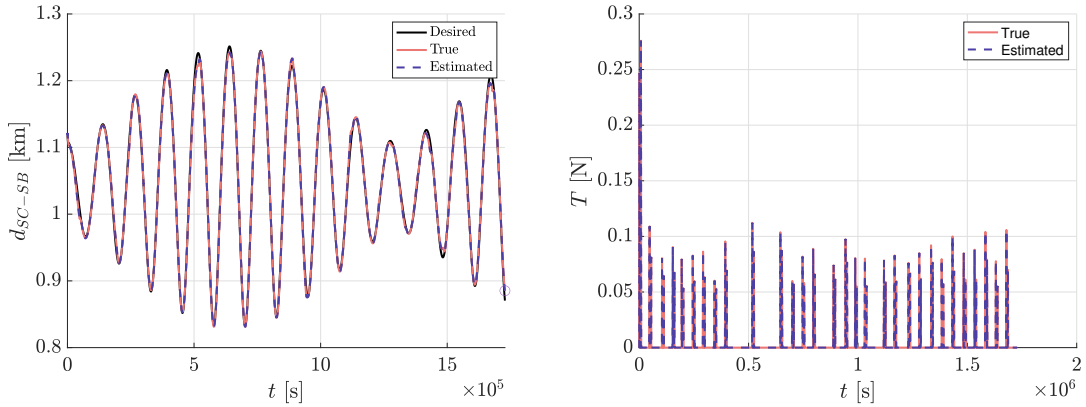

(a) (b)

Figure 12: Desired, true, and estimated distance from the asteroid (a) and true and estimated thrust profile (b) throughout the simulation.

SIMULATION RESULTS

Simulation Setup

The orbital simulation of the CubeSat around (99942) Apophis is conducted using the MuSCAT simulator, with a comprehensive setup to assess its performance over a 20-day period starting from February 1st 2029. The simulation utilized a time step of 20 seconds to capture the spacecraft orbital dynamics, with attitude estimation being performed at a more granular interval of 0.1 seconds, corresponding to the IMU update frequency. This high-resolution attitude estimation and control are carried out continuously, with the exception of periods when the spacecraft is undergoing a slew

maneuver.
Orbital determination is conducted every 10 minutes, contingent upon the asteroid being within the camera FoV. The orbital control system is designed to operate flexibly, with adjustments being made throughout the orbit as needed. Specifically, control actions are triggered when the percentage error in the spacecraft position relative to the nominal trajectory exceeds a certain percentage η of the orbital distance. For this work, values of 3% and 10% were considered.

$$||\mathbf{r}^*(t_k) - \hat{\mathbf{r}}(t_k)||_2 \geq \eta \, d_{SC-SB} \tag{57}$$

where $\mathbf{r}^*$ and $\hat{\mathbf{r}}$ are the desired and estimated position, respectively. Figure 13 shows the evolution of the CubeSat's distance from the nominal trajectory. In this example, when the error exceeds 3% of the spacecraft–small body distance, orbital control is performed to bring the CubeSat as close as possible to the nominal trajectory.

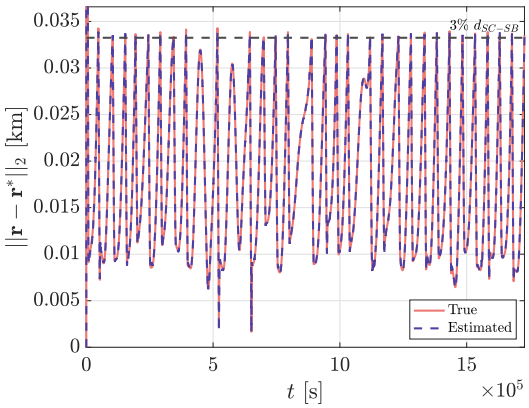

Figure 13: Orbital distance from the nominal trajectory.

This strategy allows for precise corrections and adherence to the planned trajectory. Additionally, the time interval between position and velocity control burns is fixed at 2 hours.
To thoroughly assess the CubeSat performance under various conditions, the simulation incorporates a range of thrust errors and orbital distances, with thrust errors, added to the thrust magnitude as zero-mean white Gaussian noises, defined as:

$$\epsilon_T \in \{0,\ 1e-4,\ 1e-3\}N \tag{58}$$

and orbital distances ranging from 2 to 9 small body radii, with a sampling rate of half a body radius, resulting in 15 different distances.

$$d_{SC-SB} \in \{2,\ 2.5,\ 3,\ 3.5,\ \ldots\ 8,\ 8.5,\ 9\} \times R_{SB} \tag{59}$$

The spacecraft initial attitude is assumed to be ideal, pointing towards the small body. However, an initial dispersion is considered for the position and velocity. Specifically, the position and velocity are perturbed with zero-mean Gaussian noise, where the position noise has a standard deviation of σ_{r0} and the velocity noise has a standard deviation of σ_{v0}. For this work, σ_{r0} is set to 10% of d_{SC-SB}, and σ_{v0} is set to $1 \times 10^{-6} v_0^*$, where v_0^* represents the initial desired velocity.
Due to the high number of noise sources in the simulation environment, different runs may yield varying results. To account for this variability, a Monte Carlo analysis is conducted using 10 different randomly generated seeds. Specifically, simulations are performed on the JPL high-performance computer Gattaca, which supports parallel computing and thus reduces overall computational time.

Results

The simulation results for the average time between TCMs, ΔT_{avg}, for the 3% and 10% control actions are shown in Figures 14a and 15a. Several key observations can be made from these results.

First, it can be noted that a thrust error up to 1×10^{-4} has a negligible impact on orbital evolution. The trajectory closely follows that of the zero-error case, especially as the orbital distance increases. Specifically, for the 3% case, the trajectories overlap at $5d_{SC-SB}$, while they are always coincident for the 10% case. As expected, the frequency of TCMs increases with higher thrust errors.

The temporal separation between maneuvers does not exhibit a clear increasing or decreasing trend, indeed, for the zero-error and 1×10^{-4} error cases, there is a peak in temporal separation around $3.5d_{SC-SB}$ for the 3% case. This peak can be explained by the changing dominance of different accelerations as the spacecraft moves away from the body. Near the asteroid, its gravitational influence is the predominant force, but as the spacecraft moves further away, SRP becomes increasingly significant, causing the orbits to deviate from standard Keplerian trajectories. Simultaneously, the spacecraft moves slowly along its orbit, leading to reduced error accumulation. The interplay between the body's gravity, SRP, and error accumulation leads to this observed behavior. For the 10% case, the peak shifts to the right and spreads out, with the covariance appearing more dispersed compared to the 3% case.

In contrast, for both cases, the 1×10^{-3} thrust error case scenario shows a monotonically increasing trend in the temporal separation between maneuvers as the orbital distance increases. This is because the larger thrust error plays a dominant role in causing the spacecraft to deviate from its nominal trajectory. Unlike the lower thrust error cases, where body gravity and SRP significantly influence orbital evolution, in this scenario, these accelerations have a less significant impact, as it is the thrust error that causes rapid divergence from the nominal path.

Regarding the overall mission ΔV, as shown in Figures 14b and 15b, two conclusions can be drawn. First, the thrust error does not significantly affect the overall mission cost, as the three curves nearly overlap. Second, the ΔV value increases monotonically with distance. This behavior is expected since the initial dispersion is a function of the spacecraft's orbital distance. Therefore, the first maneuver plays a crucial role in the overall ΔV consumption of the mission.

It is evident that, in the 3% case, all curves with 3σ bounds remain below the 24-hour threshold, indicating that, regardless of distance or thrust error, this control strategy consistently requires autonomy. Under these conditions, the spacecraft remains extremely close to the nominal trajectory. Notably, in the $2d_{SC-SB}$ case, the temporal separation between TCMs is nearly zero. This scenario prevents the spacecraft from pointing towards the asteroid, which disrupts the landmark tracking orbit determination method by cutting off measurements, ultimately leading to mission failure and the spacecraft crashing into the small body. Consequently, for the 3% case, the remaining figures will not include the $2d_{SC-SB}$ orbital distance.
The overall ΔV cost of the mission, as shown in Figure 14b, is around $0.005\ \mathrm{m/s}$ near the small body and increases up to $0.02\ \mathrm{m/s}$ at $9d_{SC-SB}$.

Figures 15a and 15b show the results for the 10% control case. Apart from the general observations already discussed, additional insights can be made. In this case, for thrust errors lower than 1×10^{-3}, the frequency of TCMs is always above 24 hours, indicating that autonomy is not required. Additionally, the $2d_{SC-SB}$ case functions accurately since the spacecraft has more time to slew and point towards the asteroid before exceeding the 10% error. The peak around $3.5d_{SC-SB}$, in the 3%

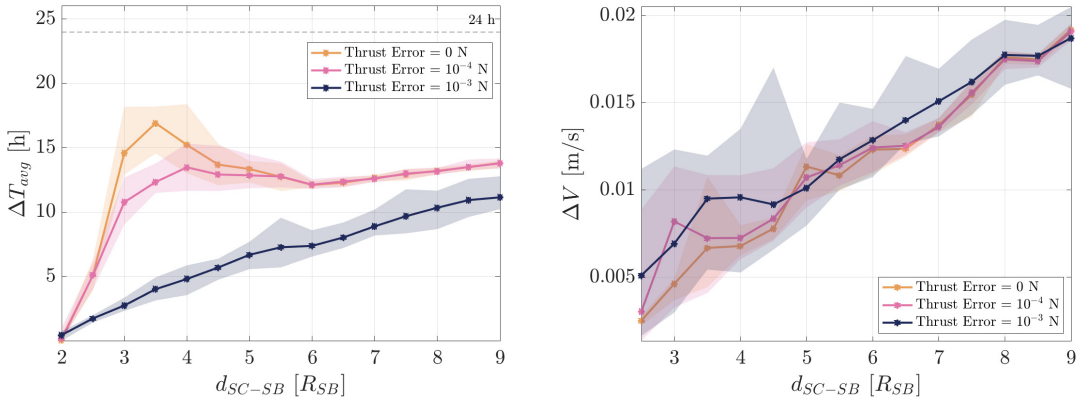

(a) Average frequency of trajectory correction maneuvers, with 3σ bounds.

(b) Overall mission cost in terms of ΔV, with 3σ bounds.

Figure 14: Frequency of TCMs and overall cost of the mission around asteroid (99942) Apophis at different distances and thrust errors for the 3% orbital control scenario.

case, broadens and can be explained by the fact that the spacecraft has more time to dynamically evolve, while the SRP does not yet significantly influence the orbit.
A significant difference from the 3% case is observed in the ΔV cost. The overall mission cost increases because the maximum distance of the spacecraft from the nominal trajectory is greater, necessitating stronger orbital control actions to correct its path. Specifically, the minimum mission cost is approximately 0.02 m/s, while the maximum reaches 0.06 m/s.

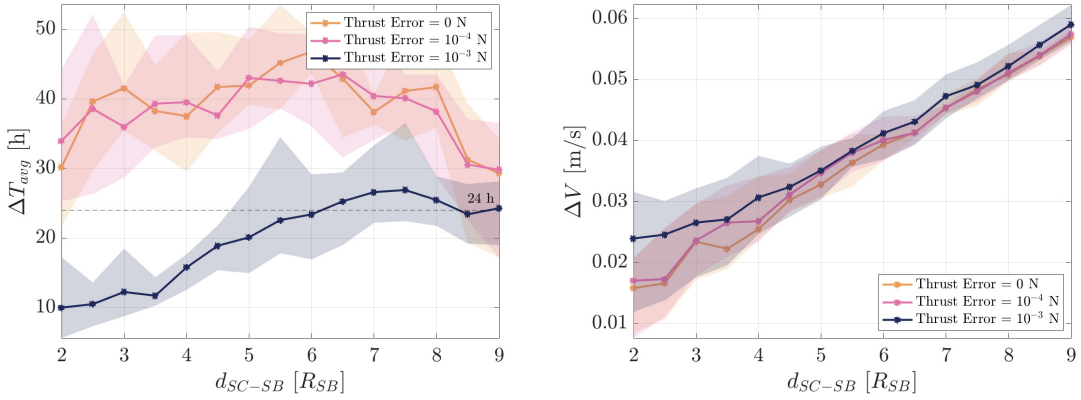

(a) Average frequency of trajectory correction maneuvers, with 3σ bounds.

(b) Overall mission cost in terms of ΔV, with 3σ bounds.

Figure 15: Frequency of TCMs and overall cost of the mission around asteroid (99942) Apophis at different distances and thrust errors for the 10% orbital control scenario.

Figures 16a and 16b show the frequency of reaction wheel desaturations. For both control strategies, the temporal distance between desaturations is around $9 - 10$ d, with a decreasing trend as the distance increases. The main observation from these plots is that the covariance for the 3% case is

more spread out compared to the 10% case. This behavior can be explained by the fact that in the 3% case, the spacecraft is slewing more frequently, leading to a higher accumulation of errors.

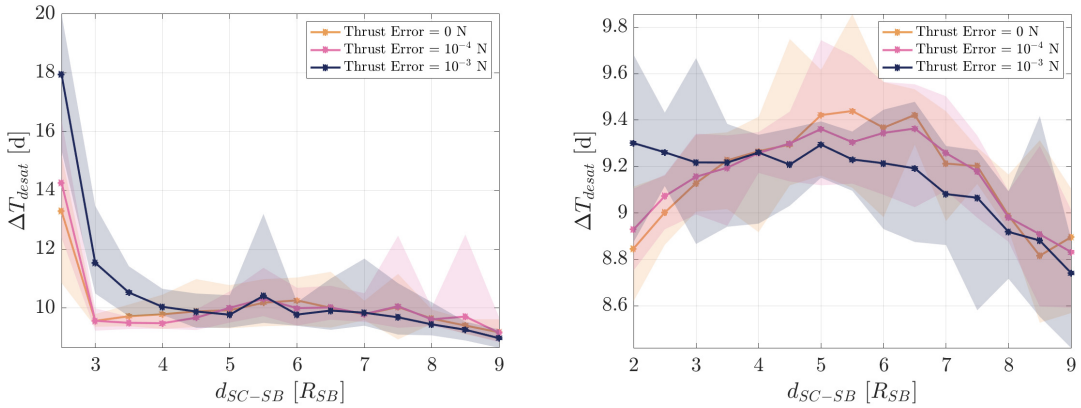

(a) 3% orbital control scenario.

(b) 10% orbital control scenario

Figure 16: Average frequency of reaction wheels desaturation around asteroid (99942) Apophis, with 3σ bounds at different distances and thrust errors.

CONCLUSIONS

Asteroid missions using resource-limited platforms like CubeSats are becoming increasingly popular. The environment near these objects is extremely challenging, requiring rapid response from the spacecraft. As a result, communication with Earth may not be feasible during close proximity operations, creating the need for autonomous algorithms. This study addresses the problem of autonomy, aiming to determine the extent to which autonomy is required for asteroid close proximity operations. The case study assumes a 6U CubeSat from the DROID mission orbiting asteroid (99942) Apophis in a quasi-terminator polar orbit at different distances and with varying thrust errors. Four state-of-the-art algorithms for attitude and orbit estimation and control were implemented and integrated into MuSCAT, a tool enabling the coupling of trajectory evolution with attitude modeling. The torque resulting from reaction wheel desaturation was also considered, with desaturation frequency shown as a function of thrust error and distance. It was found that the desaturation frequency occurs within a certain range of days, with a slight increase as the distance from the asteroid grows. Monte Carlo simulations were run considering two different orbital control strategies: one where the spacecraft can deviate up to 3% from the nominal trajectory before control, and another with a 10% deviation threshold. The results demonstrated that in the 3% case, spacecraft autonomy is required regardless of the distance and thrust error. In contrast, for the 10% case, the mission could be accomplished without autonomy, relying solely on communications with the ground operations team for lower thrust errors.

The results presented here open up several avenues for future research. Firstly, instantaneous position estimation of the spacecraft is assumed, but this is not the case in real missions, where the estimated orbit is propagated, and future control actions are planned accordingly.

In the current study, all data are assumed to reach Earth instantaneously; therefore, the data cut-off must be accurately modeled.

Lastly, the measurements in the orbit determination pipeline are simulated. An innovative image processing algorithm should be integrated and tested to evaluate performance when the target body is not perfectly known, and landmarks need to be extracted from images.

ACKNOWLEDGMENTS

The research was carried out at the Jet Propulsion Laboratory, California Institute of Technology, under a contract with the National Aeronautics and Space Administration (80NM0018D0004). © 2024. California Institute of Technology. Government sponsorship acknowledged.

The High Performance Computing resources used in this investigation were provided by funding from the JPL Information and Technology Solutions Directorate.

REFERENCES

[1] E. Asphaug, "Growth and evolution of asteroids," *Annual Review of Earth and Planetary Sciences*, Vol. 37, 2009, pp. 413–448, 10.1146/ANNUREV.EARTH.36.031207.124214.

[2] M. Quadrelli, L. Wood, J. Riedel, M. McHenry, M. Aung, L. Cangahuala, R. Volpe, P. Beauchamp, and J. Cutts, "Guidance, navigation, and control technology assessment for future planetary science missions," *Journal of Guidance, Control, and Dynamics*, Vol. 38, No. 7, 2015, pp. 1165–1186, 10.2514/1.G000525.

[3] K. Zacny, P. Chu, J. Craft, M. Cohen, W. James, and B. Hilscher, "Asteroid mining," *AIAA SPACE 2013 Conference and Exposition*, 2013.

[4] C. Buonagura, C. Giordano, F. Ferrari, and F. Topputo, "The Orbital Regime Index: a Comprehensive Parameter to Determine Orbital Regions Around Minor Bodies," *47th Rocky Mountain AAS GN&C Conference*, 2024.

[5] S. Naidu, L. Benner, M. Brozovic, M. Nolan, S. Ostro, J. Margot, J. Giorgini, T. Hirabayashi, D. Scheeres, P. Pravec, P. Scheirich, C. Magri, and J. Jao, "Radar observations and a physical model of binary near-Earth asteroid 65803 Didymos, target of the DART mission," *Icarus*, Vol. 348, 2020, p. 113777, 10.1016/j.icarus.2020.113777.

[6] R. T. Daly, C. M. Ernst, O. S. Barnouin, R. W. Gaskell, H. Nair, H. Agrusa, N. L. Chabot, A. F. Cheng, E. Dotto, E. M. Epifani, R. C. Espiritu, T. L. Farnham, E. E. Palmer, P. Pravec, A. S. Rivkin, D. C. Waller, A. Zinzi, t. DART, and L. teams, "An Updated Shape Model of Dimorphos from DART Data," *The Planetary Science Journal*, Vol. 5, No. 1, 2024, p. 24, 10.3847/PSJ/ad0b07.

[7] P. L. Lamy, I. Toth, H. Weaver, L. Jorda, M. Kaasalainen, and P. Gutiérrez, "Hubble Space Telescope observations of the nucleus and inner coma of comet 67P/Churyumov-Gerasimenko," *Astronomy & Astrophysics*, Vol. 458, No. 2, 2006, pp. 669–678, 10.1051/0004-6361:20065253.

[8] D. Lauretta, D. DellaGiustina, C. Bennett, D. Golish, K. Becker, S. Balram-Knutson, O. Barnouin, T. Becker, W. Bottke, W. Boynton, *et al.*, "The unexpected surface of asteroid (101955) Bennu," *Nature*, Vol. 568, No. 7750, 2019, pp. 55–60, 10.1038/s41586-019-1033-6.

[9] R. B. Negri, A. F. B. A. Prado, R. A. J. Chagas, and R. V. Moraes, "Autonomous Rapid Exploration in Close-Proximity of Asteroids," *Journal of Guidance, Control, and Dynamics*, Vol. 47, No. 5, 2024, pp. 914–933, 10.2514/1.G007186.

[10] J. Miller, B. Williams, W. Bollman, R. Davis, C. Helfrich, D. Scheeres, S. Synnott, T. Wang, and D. Yeomans, "Navigation analysis for Eros rendezvous and orbital phases," *Journal of the Astronautical Sciences*, Vol. 43, No. 4, 1995, pp. 453–476.

[11] J. Kawaguchi, "Hayabusa, Summary of Guidance, Navigation and Control Achievement in its Proximity Phase," *AIAA/AAS Astrodynamics Specialist Conference and Exhibit*, 2006, pp. 2006–6533, 10.2514/6.2006-6533.

[12] T. Yamaguchi, T. Saiki, S. Tanaka, Y. Takei, T. Okada, T. Takahashi, and Y. Tsuda, "Hayabusa2-Ryugu proximity operation planning and landing site selection," *Acta Astronautica*, Vol. 151, 2018, pp. 217–227, 10.1016/j.actaastro.2018.05.032.

[13] B. Williams, P. Antreasian, E. Carranza, C. Jackman, J. Leonard, D. Nelson, B. Page, D. Stanbridge, D. Wibben, K. Williams, *et al.*, "OSIRIS-REx flight dynamics and navigation design," *Space Science Reviews*, Vol. 214, 2018, pp. 1–43.

[14] P. Michel, M. Kueppers, H. Sierks, I. Carnelli, A. F. Cheng, K. Mellab, M. Granvik, M. Kestilä, T. Kohout, K. Muinonen, A. Näsilä, A. Penttila, T. Tikka, P. Tortora, V. Ciarletti, A. Hérique, N. Murdoch, E. Asphaug, A. Rivkin, O. Barnouin, A. C. Bagatin, P. Pravec, D. C. Richardson, S. R. Schwartz, K. Tsiganis, S. Ulamec, and O. Karatekin, "European Component of the AIDA Mission to a Binary Asteroid: Characterization and Interpretation of the Impact of the DART Mission," *Advances in Space Research*, Vol. 62, No. 8, 2018, pp. 2261–2272, 10.1016/j.asr.2017.12.020.

[15] M. Pugliatti, A. Rizza, F. Piccolo, V. Franzese, C. Bottiglieri, C. Giordano, F. Ferrari, and F. Topputo, "The Milani Mission: Overview and Architecture of the Optical-Based GNC System," *AIAA SCITECH 2022 Forum*, 2022.

[16] H. Goldberg, Ö. Karatekin, B. Ritter, A. Herique, P. Tortora, C. Prioroc, B. G. Gutierrez, P. Martino, and I. Carnelli, "The Juventas CubeSat in Support of ESA's Hera Mission to the Asteroid Didymos," *33rd Annual AIAA/USU Conference on Small Satellites*, 2019.

[17] D. Scheeres and J. McMahon, "Autonomous Architectures for Small Body Exploration," *AAS/AIAA Astrodynamics Specialist Conference*, 2019, pp. 19–656.

[18] C. Raymond, R. Amini, P. Adell, S. Bandyopadhyay, J. Bellerose, S. Bhaskaran, P. Bousquet, M. Calaprice, B. Davidsson, L. Fesq, *et al.*, "The Droid Mission Concept to Accompany and Characterize Apophis through its 2029 Earth Closest Approach," *LPI Contributions*, Vol. 3006, 2024, p. 2065.

[19] S. Bandyopadhyay, R. Amini, R. Miller, S. Bhaskaran, R. L. Anderson, S. Hernandez, M. Haynes, P. Adell, C. Raymond, and L. Fesq, "Integrated Science and Engineering Simulation Environment for Formation Flying Mission around Small Body," *IEEE Aerospace Conference*, 2023, pp. 1–8, 10.1109/AERO55745.2023.10115676.

[20] S. Takahashi and D. J. Scheeres, "Autonomous exploration of a small near-earth asteroid," *Journal of Guidance, Control, and Dynamics*, Vol. 44, No. 4, 2021, pp. 701–718, 10.2514/1.G005733.

[21] R. Furfaro, D. Cersosimo, and D. R. Wibben, "Asteroid precision landing via multiple sliding surfaces guidance techniques," *Journal of Guidance, Control, and Dynamics*, Vol. 36, No. 4, 2013, pp. 1075–1092, 10.2514/1.58246.

[22] R. Furfaro, "Hovering in Asteroid Dynamical Environments Using Higher-Order Sliding Control," *Journal of Guidance, Control, and Dynamics*, Vol. 38, No. 2, 2015, pp. 263–279, 10.2514/1.G000631.

[23] M. Vetrisano and M. Vasile, "Autonomous navigation of a spacecraft formation in the proximity of an asteroid," *Advances in Space Research*, Vol. 57, No. 8, 2016, pp. 1783–1804, 10.1016/j.asr.2015.07.024.

[24] J. Gil-Fernandez and G. Ortega-Hernando, "Autonomous vision-based navigation for proximity operations around binary asteroids," *CEAS Space Journal*, Vol. 10, 2018, pp. 287–294, 10.1007/s12567-018-0197-5.

[25] I. A. Nesnas, B. J. Hockman, S. Bandopadhyay, B. J. Morrell, D. P. Lubey, J. Villa, D. S. Bayard, A. Osmundson, B. Jarvis, M. Bersani, *et al.*, "Autonomous exploration of small bodies toward greater autonomy for deep space missions," *Frontiers in Robotics and AI*, Vol. 8, 2021, p. 650885, 10.3389/frobt.2021.650885.

[26] A. S. French, Y. Takahashi, R. L. Anderson, S. Bhaskaran, S. Bandyopadhyay, and R. Amini, "Navigating a Dual-Spacecraft Bistatic Radar Around an Asteroid," *33rd AAS/AIAA Space Flight Mechanics Meeting*, 2023.

[27] J. D. Giorgini, L. A. Benner, S. J. Ostro, M. C. Nolan, and M. W. Busch, "Predicting the Earth encounters of (99942) Apophis," *Icarus*, Vol. 193, No. 1, 2008, pp. 1–19, https://doi.org/10.1016/j.icarus.2007.09.012.

[28] M. Brozović, L. A. Benner, J. G. McMichael, J. D. Giorgini, P. Pravec, P. Scheirich, C. Magri, M. W. Busch, J. S. Jao, C. G. Lee, *et al.*, "Goldstone and Arecibo radar observations of (99942) Apophis in 2012–2013," *Icarus*, Vol. 300, 2018, pp. 115–128, 10.1016/j.icarus.2017.08.032.

[29] P. Pravec, P. Scheirich, J. Ďurech, J. Pollock, P. Kušnirák, K. Hornoch, A. Galád, D. Vokrouhlický, A. Harris, E. Jehin, J. Manfroid, C. Opitom, M. Gillon, F. Colas, J. Oey, J. Vraštil, D. Reichart, K. Ivarsen, J. Haislip, and A. LaCluyze, "The tumbling spin state of (99942) Apophis," *Icarus*, Vol. 233, 2014, pp. 48–60, https://doi.org/10.1016/j.icarus.2014.01.026.

[30] S. Bandyopadhyay, Y. K. Nakka, L. Fesq, and S. Ardito, "Design and Development of MuSCAT: Multi-Spacecraft Concept and Autonomy Tool," *AIAA AVIATION FORUM AND ASCEND 2024*, 2024, p. 4805.

[31] S. Bandyopadhyay, "Multi-Spacecraft Concept and Autonomy Tool (MuSCAT)," 2024. [cited September 4, 2024].

[32] S. Bandyopadhyay, Y. K. Nakka, L. Fesq, and S. Ardito, "Design and Development of MuSCAT: Multi-Spacecraft Concept and Autonomy Tool," *AIAA Accelerating Space Commerce, Exploration, and New Discovery (ASCEND)*, 2024, pp. 24–99. In press.

[33] D. Bayard, "High-Precision Three-Axis Pointing and Control," 12 2010, 10.1002/9780470686652.eae300.

[34] J. Darling, N. Houtz, C. Frueh, and K. J. DeMars, "Recursive Filtering of Star Tracker Data," *AIAA/AAS Astrodynamics Specialist Conference*, 2016, 10.2514/6.2016-5672.

[35] F. L. Markley and J. L. Crassidis, *Fundamentals of Spacecraft Attitude Determination and Control*. New York: Microcosm Press and Springer, 1 ed., 2014, 10.1007/978-1-4939-0802-8.

[36] S. Bandyopadhyay, S.-J. Chung, and F. Y. Hadaegh, "Nonlinear Attitude Control of Spacecraft with a Large Captured Object," *Journal of Guidance, Control, and Dynamics*, Vol. 39, No. 4, 2016, pp. 754–769, 10.2514/1.G001341.

[37] R. H. Battin, *Solving Lambert's Problem*, ch. Chapter 7, pp. 295–364. AIAA, 1999, 10.2514/5.9781600861543.0295.0364.